Baryon-driven decontraction in Milky Way-mass haloes

Victor J. Forouhar Moreno [ORCID],[1][*] Alejandro Benítez-Llambay [ORCID],[2] Shaun Cole[1] and Carlos Frenk[1]

[1]*Institute for Computational Cosmology, Department of Physics, Durham University, Durham DH1 3LE, UK*
[2]*Dipartimento Di Fisica "Giuseppe Occhialini", University of Milano-Bicocca, Piazza della Scienza, 3, 20126 Milano MI, Italy*

ABSTRACT

We select a sample of Milky Way (MW) mass haloes from a high-resolution version of the EAGLE simulation to study their inner dark matter (DM) content and how baryons alter it. As in previous studies, we find that all haloes are more massive at the centre compared to their dark matter-only (DMO) counterparts at the present day as a result of the dissipational collapse of baryons during the assembly of the galaxy. However, we identify two processes that can reduce the central halo mass during the evolution of the galaxy. First, gas blowouts induced by active galactic nuclei feedback can lead to a substantial decrease of the central DM mass. Secondly, the formation of a stellar bar and its interaction with the DM can induce a secular expansion of the halo; the rate at which DM is evacuated from the central region by this process is related to the average bar strength, and the time-scale on which it acts determines how much the halo has decontracted. Although the inner regions of the haloes we have investigated are still more massive than their DMO counterparts at $z = 0$, they are significantly less massive than in the past and less massive than expected from the classic adiabatic contraction model. Since the MW has both a central supermassive black hole and a bar, the extent to which its halo has contracted is uncertain. This may affect estimates of the mass of the MW halo and of the expected signals in direct and indirect DM detection experiments.

Key words: dark matter – galaxies: bar – galaxies: evolution.

1 INTRODUCTION

Structure formation in a cold dark matter (CDM) universe proceeds in a hierarchical bottom-up manner. Small-scale overdensities are the first to decouple from the Hubble flow and undergo gravitational collapse. Their subsequent growth is driven by mergers with neighbouring structures and diffuse, smooth mass accretion from the surroundings. The end result is a bound, virialized halo of dark matter (DM) that can host a galaxy at its centre if it is massive enough (White & Rees 1978; Benitez-Llambay & Frenk 2020). *N*-body simulations that model the DM and baryons as a single collisionless fluid predict DM density profiles with shapes that are roughly independent of halo mass, cosmological parameters, and the primordial fluctuation power spectrum (Navarro, Frenk & White 1996b; Wang et al. 2020). These density profiles are well fitted by the two-parameter Navarro–Frenk–White (NFW; Navarro et al. 1996b; Navarro, Frenk & White 1997) profile:

$$\rho_{\rm NFW}(r) = \frac{\rho_0}{\frac{r}{r_{\rm s}}\left(1 + \frac{r}{r_{\rm s}}\right)^2} \,, \qquad (1)$$

although more recent, higher resolution simulations suggest that the three-parameter Einasto (1965) profile provides an even better fit (Navarro et al. 2004). The two parameters of the NFW profile are related to the halo virial mass and its concentration, both of which are tightly correlated. This is a consequence of the mass dependence of the formation epoch of haloes, as a result of which less-massive haloes typically have greater concentrations than more massive ones, reflecting the fact that they undergo gravitational collapse earlier, when the universe was correspondingly denser.

The ubiquitous prediction of centrally divergent halo density profiles in CDM offers a test of whether DM is cold or not. This has motivated numerous studies comparing observations of the inferred DM density profiles to theoretical predictions on a wide range of scales, from dwarf galaxies (e.g. Burkert 1995; Strigari, Frenk & White 2010; Walker & Peñarrubia 2011; Agnello & Evans 2012; Oh et al. 2015) to rich galaxy clusters (e.g. Sand, Treu & Ellis 2002; Umetsu & Diemer 2017; He et al. 2020). The comparisons are largely based on predictions stemming from purely collisionless dark matter-only (DMO) *N*-body simulations, where non-linear effects produced by baryons are unaccounted for. Processes associated with the formation and evolution of galaxies can have measurable effects on the structure of the DM haloes hosting them, such as changing the distribution of DM or redistributing angular momentum (e.g. Zavala, Okamoto & Frenk 2008; Chan et al. 2015; Schaller et al. 2015). The increasing availability of hydrodynamical cosmological simulations able both to reproduce many measured galaxy population statistics and have sufficient resolution to probe the galaxy-scale distribution of DM enables a more meaningful comparison between theory and observations (for a review, see Somerville & Davé 2015). These simulations use subgrid prescriptions to model processes such as star formation, gas cooling, and feedback due to supernovae and active galactic nuclei (AGN). The interplay between these processes leads to a complex and rich phenomenology that is missing in DMO simulations.

Initially, gas near a growing DM halo is dragged in due to the deepening gravitational potential well, shock heated and, if it can cool

efficiently, it will sink towards the centre where star formation can commence once the gas density is large enough (White & Rees 1978). The dissipative collapse of gas and its assembly in the central regions of the halo deepens the potential well, inducing a contraction of the DM halo and enhancing the central density compared to the DMO counterpart. The effectiveness of this response depends on a number of properties, such as the mass of the central galaxy, the assembly history of the halo, and the phase-space distribution of DM particles (Abadi et al. 2010; Dutton et al. 2016; Artale et al. 2019). The first analytical models used to estimate this response assumed 'adiabatic contraction' and circular orbits (Blumenthal et al. 1986; Ryden & Gunn 1987) but were later expanded to take into account the orbital eccentricities of typical DM particles (Gnedin et al. 2004). More recently, there have been a number of extensions based on empirical fits to the measured response in hydrodynamical *N*-body simulations (Cautun et al. 2020), as well as orbital phase-space modelling using integrals of motion (Callingham et al. 2020).

The assembly of gas and stars has other effects that are in direct competition with the contraction of the halo. The sudden expulsion, driven by supernovae explosions, of gas that had previously accumulated slowly at the centre of a dwarf galaxy halo can cause the central regions of the halo to expand (Navarro, Eke & Frenk 1996a). This can occur in a single disruptive event or in a series of more moderate perturbations that drive oscillations in the gravitational potential (Read & Gilmore 2005; Pontzen & Governato 2014). On cluster scales, a similar outcome can result from powerful AGN-driven outbursts (Martizzi, Teyssier & Moore 2013). Similarly, dynamical friction exerted on infalling gas clumps by dwarf-scale haloes (El-Zant, Shlosman & Hoffman 2001; Mashchenko, Couchman & Wadsley 2006) or merging galaxies in cluster-scale haloes (El-Zant et al. 2004; Laporte et al. 2012) could also lower the central DM density.

The details of how star formation is modelled determines the degree of gravitational coupling between the gas and the DM halo, and thus influences how effectively gas blowouts can alter the inner contents of DM haloes (Benítez-Llambay et al. 2019). This explains differences in the predicted density profiles of dwarf galaxies between simulations employing high-density thresholds and those employing lower ones. Whilst the former are able to accumulate sufficient quantities of gas in the central regions of the halo prior to the gas being blown out, low-density thresholds never reach this point. Another important aspect of gravitational perturbations is the time-scale on which they operate. As discussed in the appendix of Benítez-Llambay et al. (2019), perturbations that last longer, compared to the typical dynamical time of the shell, remove DM more effectively. If the perturbation time-scale is sufficiently long, the effectiveness of each individual perturbation in heating the DM becomes maximal. This means that the integrated effect is solely dependent on the number of such perturbations.

Finally, torques exerted by non-axisymmetric features are able to redistribute angular momentum between baryons and DM, as well as within the galaxy itself (Lynden-Bell & Kalnajs 1972; Lynden-Bell 1979). One example are stellar bars, which are present in a significant fraction of nearby spiral galaxies (Eskridge et al. 2000; Sheth et al. 2008; Skibba et al. 2012; Buta et al. 2015) and in our own Milky Way (MW; Binney et al. 1991; Weiland et al. 1994; Dwek et al. 1995; Ness et al. 2016). The formation of a bar can be driven by an instability resulting from a kinematically cold and gravitationally important disc, as appreciated in early *N*-body simulations (e.g. Miller, Prendergast & Quirk 1970; Hohl 1971). An alternative bar-formation mechanism relies on external triggers such as tidal interactions caused by a close flyby or a merger (Noguchi

1987; Łokas et al. 2016; Martinez-Valpuesta et al. 2017). These processes can also reconstitute previously existing bars (Berentzen et al. 2004).

The subsequent evolution of the bar is determined by exchange of angular momentum, which can lead to its strengthening and lengthening (Athanassoula 2003). This exchange occurs near orbital resonances. While some authors argue that as many as 10^8 particles are required to model the resonances (e.g. Ceverino & Klypin 2007; Weinberg & Katz 2007a,b), others find less-stringent conditions on the grounds that a time-evolving bar pattern speed broadens the resonant regions (e.g. Sellwood 2006). The net flow of angular momentum depends on the dynamical and spatial properties of the constituent components of the system (for a review, see Athanassoula 2013). The regions of the disc within the corotation radius of a bar lose it, whereas those beyond gain it. On the other hand, spheroidal components such as the DM halo and the stellar bulge are only able to acquire it. Consequently, bar-driven changes in the distribution of angular momentum can change the structural properties of discs (Debattista et al. 2006), cause classical bulges to acquire net rotation (Saha, Martinez-Valpuesta & Gerhard 2012; Kataria & Das 2019) and alter the central density of DM haloes (Weinberg & Katz 2002; Holley-Bockelmann, Weinberg & Katz 2005; Sellwood 2008; Dubinski, Berentzen & Shlosman 2009; Algorry et al. 2017).

The efficiency with which all these different processes are able to alter the central density of DM depends largely on the mass scale under consideration. For example, the small amount of baryons collected at the centre of very faint dwarfs cannot alter significantly the inner DM content of their host halo. On the other hand, if too many baryons end up locked in stars in larger haloes, the DM contracts in response to them. There is thus a narrow range in mass in which supernovae-driven gas blowouts are effective at driving DM mass out (e.g. Di Cintio et al. 2014; Tollet et al. 2016). It is then common practice to assume that larger haloes, particularly those with mass comparable to that of our MW, are only subject to the contraction caused by baryons, ignoring altogether the competing effects caused by other processes, such as AGN-driven outflows of gas, or the presence of a massive bar at the centre.

In this paper, we revisit these ideas using a high-resolution hydrodynamical simulation of the EAGLE project. In particular, we study in detail the time evolution of the inner DM content of a sample of MW-mass haloes and search for events that alter it. Understanding the role of baryons in these haloes is important for a wide range of applications, from mass estimates of our MW (Cautun et al. 2020) to informing direct and indirect searches for DM (Calore et al. 2015; Bozorgnia et al. 2016; Schaller et al. 2016; Bozorgnia & Bertone 2017).

The paper is structured as follows. Section 2 describes the simulations as well as our selection of a sample of galaxies for analysis. Section 3 presents our results, focusing first on gas blowouts and then on stellar bars, as well as on the resulting contraction and expansion of the central regions of the halo. Our conclusions are presented in Section 4.

2 SIMULATIONS

In this section, we give an overview of the EAGLE simulations used in this work and describe the selection of our halo sample.

2.1 The code

The EAGLE project (Crain et al. 2015; Schaye et al. 2015) is a suite of hydrodynamical cosmological simulations that follow the

formation and evolution of cosmic structure from ΛCDM initial conditions assuming the cosmological parameter values from Planck Collaboration I (2014). They were performed using a modified version of the P-Gadget3 code (Springel 2005) that incorporates subgrid prescriptions for the physics relevant to galaxy formation and evolution: radiative cooling (Wiersma, Schaye & Smith 2009), photoheating, star formation and evolution (Schaye 2004; Schaye & Dalla Vecchia 2008), stellar feedback (Dalla Vecchia & Schaye 2012), black hole seeding (Springel, Di Matteo & Hernquist 2005; Booth & Schaye 2009), its subsequent growth, and stochastic, thermal AGN feedback. The values of the parameters used in modelling these processes were set by requiring a good match to the observed $z = 0.1$ galaxy stellar mass function, the distribution of galaxy sizes, and the amplitude of the central black hole mass *versus* stellar mass relation. Once calibrated in this way, EAGLE reproduces a number of population statistics (Schaller et al. 2015; Ludlow et al. 2017).

In this work, we use the higher mass resolution version of EAGLE (see Crain et al. 2015 for details), in which the subgrid physics parameters were recalibrated to account for the increased mass resolution. This simulation follows 2×752^3 particles in a volume 25 Mpc on a side. This resolution corresponds to DM and gas particle masses of 1.21×10^6 M$_\odot$ and 2.26×10^5 M$_\odot$, respectively. The maximum physical Plummer-equivalent gravitational softening length is 325 pc. There are a total of 405 temporal outputs between redshifts $z = 20$ and $z = 0$, corresponding to a time resolution of $\sim$60 Myr. This provides adequate time resolution to study the processes of interest in this work.

To identify cosmic structures, we assign particles into distinct groups according to the friends-of-friends (FoF) percolation algorithm (Davis et al. 1985). Each group is made up of particles that are within 0.2 times the mean interparticle separation from one another. Gravitationally bound substructure is found with the SUBFIND algorithm (Springel et al. 2001), which, using particle velocity and position information, identifies self-bound structures within a larger FoF group. We follow the time evolution of the SUBFIND groups by identifying their main progenitor. This is achieved by cross-matching a subset of the most bound particles between consecutive time outputs.

2.2 Sample selection

Since we are interested in the central parts of DM haloes similar to the MW's, we restrict our analysis to haloes of mass M_{200}[1] at $z = 0$ in the range $0.5-2.5 \times 10^{12}$ M$_\odot$. This encompasses recent observational estimates of the MW's halo mass (Callingham et al. 2019; Cautun et al. 2020). A total of 45 haloes satisfying this criterion were identified in the hydrodynamical simulation. Their stellar masses are shown in the top panel of Fig. 1. The central galaxies exhibit a wide range of masses; most are more massive than 10^{10} M$_\odot$, but they are typically less massive than the MW. This is because the stellar mass to halo mass relation in EAGLE falls short in the halo mass range of interest, compared to abundance matching results (e.g. Moster, Naab & White 2013). This is related to an underestimate of the galaxy stellar mass function around the knee (Schaye et al. 2015).

Their DMO counterparts were found using the particle ID information for a subset of the most bound particles in the hydrodynamical and DMO simulations. The halo centres were found using the

---

[1]M_{200} is defined as the mass contained within a sphere of mean density 200 times the critical density of the universe.
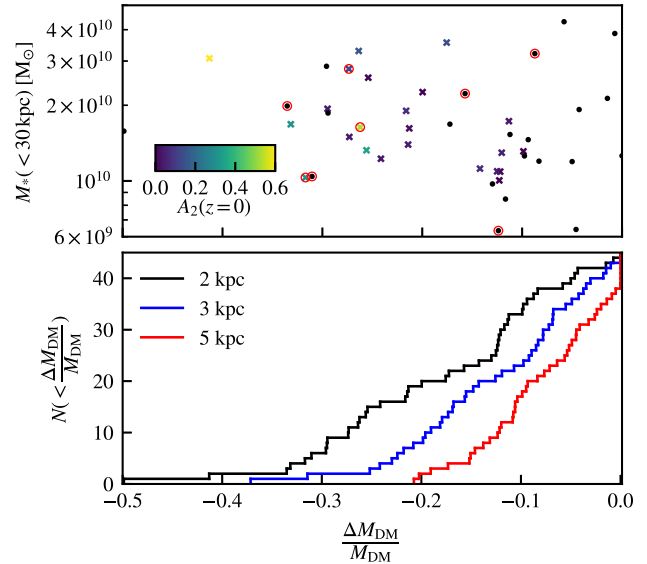
Figure 1. The top panel shows the stellar mass of the central galaxies in the selected halo sample, measured within a spherical aperture of 30 kpc, as a function of the fraction of DM mass-loss within 2 kpc of the halo centre, $M_{DM}(z = 0)/M_{DM}(z_{peak}) - 1$. The crosses indicate haloes that exhibit a monotonic decrease in mass with time; the dots are the rest of the halo sample. The former are colour coded according to how prominent their stellar bars are at $z = 0$, measured using the method described in Section 3.3. Galaxies that experienced major AGN outbursts at least once during their evolution are highlighted by the red circles. The bottom panel shows the cumulative distribution of the fractional mass-loss in the same halo sample, measured within spherical apertures of 2 kpc (black), 3 kpc (blue), and 5 kpc (red). Note that fewer haloes experience a mass-loss when considering larger apertures, hence why the y-axis intercept of the bottom panel changes.

shrinking-spheres algorithm (Power et al. 2003), run only on the DM particle distribution.

3 RESULTS

We begin with an overview of the central DM mass evolution of the selected halo sample. This is followed by a qualitative assessment at the evolution of four different haloes that illustrate the variety of baryon processes that change their innermost DM and stellar content. Finally, we discuss and characterize each of these processes, namely, an initial halo contraction due to the accumulation of baryons at the centre, which can then be followed by an expansion caused by AGN-induced gas blowouts, stellar bars, or a combination of both.

3.1 Overview

To determine whether there has been a decrease in the central mass of DM over time, we follow its time evolution within several apertures. The evolution within a 2 kpc aperture is shown for a few examples in Fig. 2. We locate the time when the DM content peaks and compare it to the present-day value. To this end we define the fractional mass-loss as $\Delta M_{DM}/M_{DM} \equiv M_{DM}(z = 0)/M_{DM}(z_{peak}) - 1$. To prevent fluctuations caused by merger events, which can cause the DM mass to fluctuate for a short period of time, we apply a linear Sagvol–Kolmogorov convolution to smooth out the evolution. We only consider peaks that are not immediately followed by a local minimum. This helps prevent transient peaks caused by mergers with other haloes, which would otherwise boost the value of $\Delta M_{DM}/M_{DM}$.
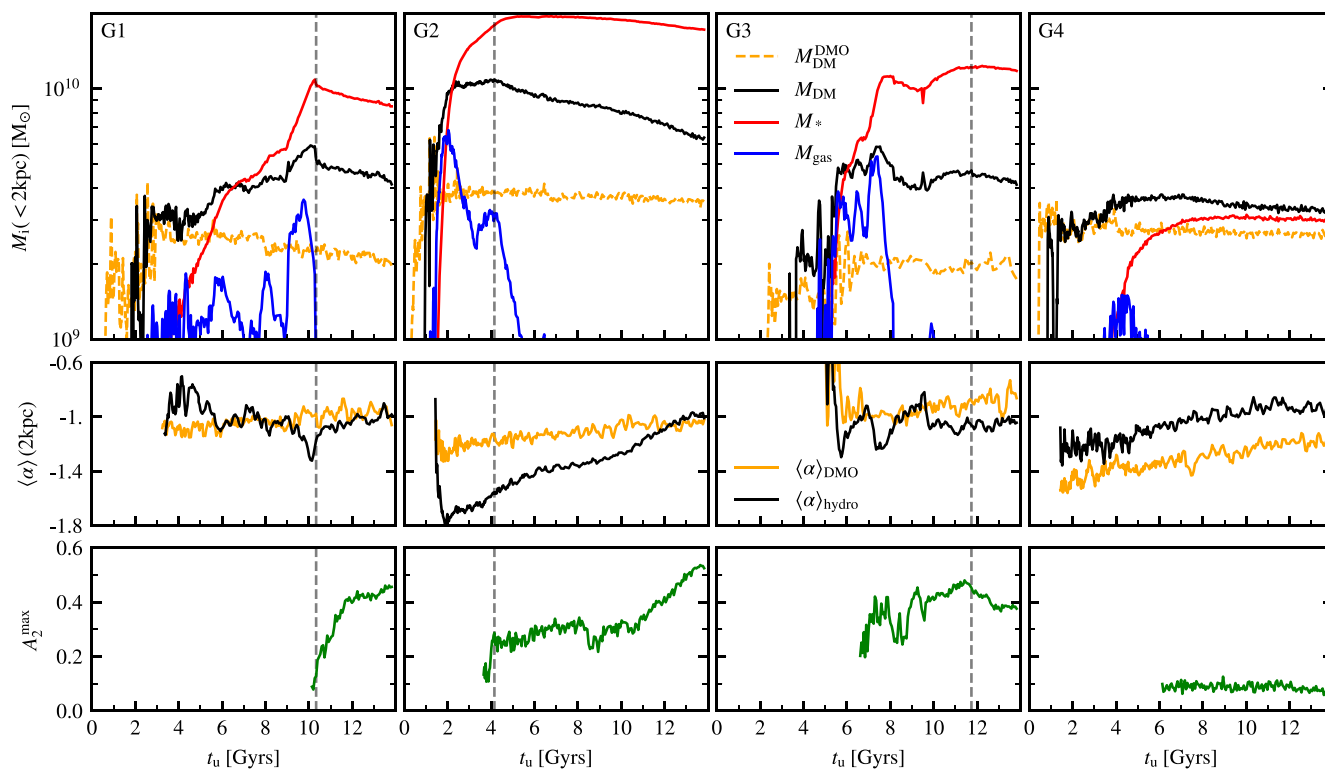
Figure 2. Time evolution of the central DM, gas, and stellar content of four MW-mass haloes, together with the evolution of their measured bar strengths. Each column is for a different halo, with the top panels showing the enclosed DM (black), gas (blue), and stellar (red) masses within a 2 kpc spherical aperture. For comparison, the DM mass enclosed within 2 kpc in the DMO counterpart is shown by the dashed orange line. The middle panels show the (smoothed) evolution of the DM density profile slope at 2 kpc, both for the DMO (orange) and hydrodynamical (black) counterparts. The bottom panels show the time evolution of the bar strength of these galaxies. For haloes G1 and G2, this is only shown from times shortly before a visually recognizable bar had formed. Halo G3 had large values of $A_2^{\max}$ even before an established bar formed, which happened shortly before the observed peak in enclosed DM mass. Halo G4 never formed a bar, hence the low values of A_2. The vertical dashed lines indicate the times used to determine $M_{\rm DM}(z_{\rm peak})$.

In practice, this may underestimate the expansion for a subset of haloes, as illustrated by halo G3 in Fig. 2, for which the local maximum at $t_{\rm u} \sim 11$ Gyr is used instead of the global maximum at $t_{\rm u} \sim 7.5$ Gyr.

The bottom panel of Fig. 1 shows the cumulative number of simulated MW-mass haloes that have lost a fractional mass $<f$ within three different spherical apertures: 2, 3, and 5 kpc. Clearly, the mass-loss does not depend on the galaxy stellar mass, as demonstrated in the top panel of the same figure. Although there is a wide range of fractional mass-loss values, no halo has lost more than 50 per cent of its peak DM mass, even within 2 kpc from the centre. Nonetheless, half of all haloes have lost more than 16 per cent of their peak DM mass within 2 kpc, with only one reaching the peak at $z = 0$. The DM mass-loss decreases when considering larger apertures: Half of the haloes considered here lose more than 11 per cent and 7 per cent their peak DM mass within 3 and 5 kpc, respectively. Nonetheless, there are still a number of haloes that exhibit a more significant decrease (~ 20 per cent) of DM mass even at 5 kpc. To investigate the reason behind the expansion, we follow the evolution of the DM halo and its associated central baryonic content.

Four representative examples are shown in Fig. 2, where the time evolution of the halo DM, gas, and stellar mass within 2 kpc are shown in the top panels by different colour lines, as indicated in the legend. These examples are chosen to illustrate the diverse evolution of the mass content that characterizes the haloes in our sample. Some exhibit only a secular decrease of DM mass over time (G2); others experience an additional, sudden mass-loss event (G1). There are

those that remain virtually unaltered throughout their lifetime (G4) and those which have a more complicated assembly history (G3). Their evolution is compared to their DMO counterparts, whose inner DM content, $M_{\rm DM}^{\rm DMO} = (1 - f_{\rm b})M_{\rm tot}^{\rm DMO}$, is shown by the black dashed lines.

In all cases, the relative difference between the enclosed DM in the hydrodynamical and DMO versions of the same haloes evolves with time. Their values are similar at large redshifts, but start to diverge once gas and stars populate the inner regions of haloes. This is evidence for the contraction of the halo induced by baryons. By $z = 0$, all the haloes in the hydrodynamical simulation are more massive at the centre than their DMO twins. Nonetheless, it is evident from haloes G1, G2, and G3 that their central DM mass in the hydrodynamical simulation evolves non-monotonically, leading to a decontraction at late times. We measure the slope of the DM density profile by fitting a power law, $\rho \propto r^\alpha$, to its central distribution. The time evolution of this quantity is shown in the middle panels of Fig. 2. None of the haloes considered here show signs of a significant flattening at ~ 2 kpc, indicating that neither AGN nor bars make cores on these scales in our simulations Moreover, there is very little difference in the slopes between the hydrodynamical and DMO versions of the same halo, despite large differences in the enclosed mass at 2 kpc. The local density slope is not an adequate metric for quantifying how contracted a halo is.

Although the physical mechanisms driving these mass changes will be discussed in detail in the following subsections, we present here a qualitative discussion on the evolution of the haloes shown in

Fig. 2, which helps understand their relative importance. As shown in the leftmost panel, the central DM and stellar masses of halo G1 peak at $t_u \sim 10.3$ Gyr. This is followed by a sudden 15 per cent and 5 per cent decrease in DM and stellar mass, respectively, and a bar forms immediately after that. The bar is associated with the start of the secular DM and stellar mass-loss from the central regions that lasts until the present day. Overall, this constitutes a total loss of 29 per cent (21 per cent) of the peak DM (stellar) mass, with the AGN responsible for 50 per cent (21 per cent) of this decrease and the stellar bar for the remainder. Halo G3 also experiences a disruptive AGN-driven gas blowout, but contrary to halo G1, its bar forms before the blowout occurs. The only mechanism responsible for the DM loss in the hydrodynamical counterpart of halo G2 is the presence of the stellar bar. Similarly to the previous examples (G1 and G3), the formation of the bar in halo G2 at $t_u \sim 4$ Gyr is associated with the onset of the secular DM and stellar mass-loss. Finally, halo G4 never forms a bar nor experiences a major gas blowout, and its inner DM mass remains roughly constant up to redshift $z = 0$.

3.2 AGN-driven gas blowouts

As we have shown in the previous section, strong gas blowouts caused by AGN activity are able to induce a substantial decrease in the central stellar and DM masses. Haloes G1 and G3 experience such blowouts, as evidenced by the sharp decrease in their enclosed stellar and DM masses shown in the top panels of Fig. 2. These occur at different times, with the blowout in halo G1 taking place at $t_u \sim$ 10.3 Gyr and that in halo G3 at $t_u \sim 8$ Gyr.

In halo G1, we can see a steady decrease of ~ 50 per cent of the gas mass in the central regions before the proper blowout that removes the remaining gas occurs (see vertical dashed line). This prior decrease is associated with star formation and stellar feedback, which, as we have verified visually, does not disrupt the gas disc. In fact, despite this decrease in gas mass, the gas disc becomes more compact and reaches a surface density comparable to that of the stellar disc just before it is disrupted. This 'compactification' could be caused by the torques exerted by the galaxy that flew by earlier (Blumenthal & Barnes 2018). Finally, a significant amount of gas mass is fed into the central black hole, triggering an outburst of AGN feedback that destroys the gas disc and removes virtually all gas from the central regions. A similar process occurs in halo G3, although this galaxy is already strongly barred prior to the AGN-driven blowout event. The bar could provide another mechanism to facilitate the inflow of gas towards the centre of the galaxy (e.g. Sanders & Huntley 1976; Fanali et al. 2015).

A requirement for blowouts to be effective in altering the distribution of DM is that gas must be strongly gravitationally coupled to the DM prior to the blowouts (Benítez-Llambay et al. 2019). We have checked whether this is the case for halo G1 by comparing the gravitational force exerted by the gas and the stars along a random azimuthal direction contained within the mid-plane of the galaxy. The leftmost top panel of Fig 2 shows that baryons dominate the central regions of halo G1. Therefore, to assess the importance of gas for the gravitational force, we only need to determine the relative contribution between the gas and stellar components. We compute the force by taking the gradient of the gravitational potential calculated by direct summation over all particles within 30 kpc from the centre of the halo. The choice of azimuthal direction has little effect on the estimated forces during the time of interest, given that there is no prominent non-axisymmetric feature prior to the blowout.

Fig. 3 shows the temporal evolution of the gravitational force exerted by the gas, relative to that of the stars, as a function of the
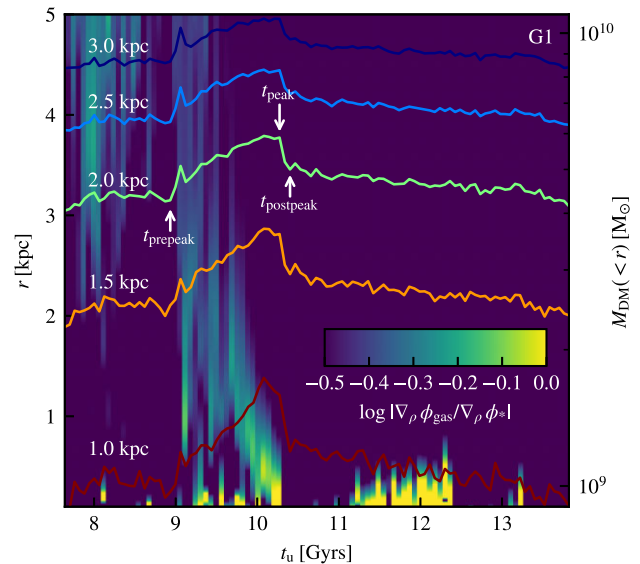
Figure 3. The colour scale indicates the ratio between the gravitational accelerations exerted by the gas relative to the stars, $\nabla_\rho \phi_{gas}/\nabla_\rho \phi_*$, along a random azimuthal direction contained within the mid-plane of the galaxy of halo G1. This is shown as a function of time (*x*-axis) and distance to the centre of the halo (*y*-axis). The solid lines show the evolution of the enclosed DM mass within spherical apertures ranging from 1 to 3 kpc, in increments of 0.5 kpc, as indicated by the labels on the left-hand side. The vertical white arrows indicate the visually determined times used to quantify the contraction and expansion of both the DM halo and the stellar component caused by changes in the gas disc.

distance to the centre. Focusing on the times prior to the blowout (9 Gyr $\leq t_u \leq$ 10.3 Gyr), the gas makes a contribution similar to the stars in the innermost regions. This is not the case for most of the evolution at late times since there is very little gas left after the blowout. Initially, the gravitational contribution of the gas disc is significant (but not dominant) throughout the central 5 kpc of the halo. The gas becomes increasingly gravitationally important in the central regions over time. As mentioned before, this is due to the fact that the gas disc becomes more compact during this time. Just before the blowout occurs, the density of the gas disc and the enclosed DM and stellar masses peak, which indicates that the baryonic blowout is responsible for the accompanying mass-loss in all the components.

We have explicitly checked that the large-scale winds are driven by AGN. Three images of the gas content of the galaxy before, during, and after the outburst are shown in Fig. 4. Prior to the start of the event, most gas is concentrated in the centre of the halo, where the black hole resides. It has a net negative average radial velocity, corresponding to inflow that is manifest in the compactification of the gas component observed in Fig. 3. Once the outburst commences, most gas is quickly evacuated from the centre in just ~ 120 Myr, with outflow velocities that are in excess of 100 km s^{-1} during the later stages.

Although the gas disc is gravitationally dominant only in the very central regions prior to being blown out, the sudden gas blowout has a measurable effect even at radii several times larger, well beyond where the gravitational contribution of the gas is significant. The solid lines in Fig. 3 show the evolution in time of the enclosed DM mass within apertures ranging from 1 to 3 kpc. Although the decrease in DM mass is larger at smaller radii, where the gravitationally coupling between the DM and the gas was larger, it is still detectable at larger radii. This also underlines the importance of the time-scale over which gravitational perturbations act. The long time-scale that it
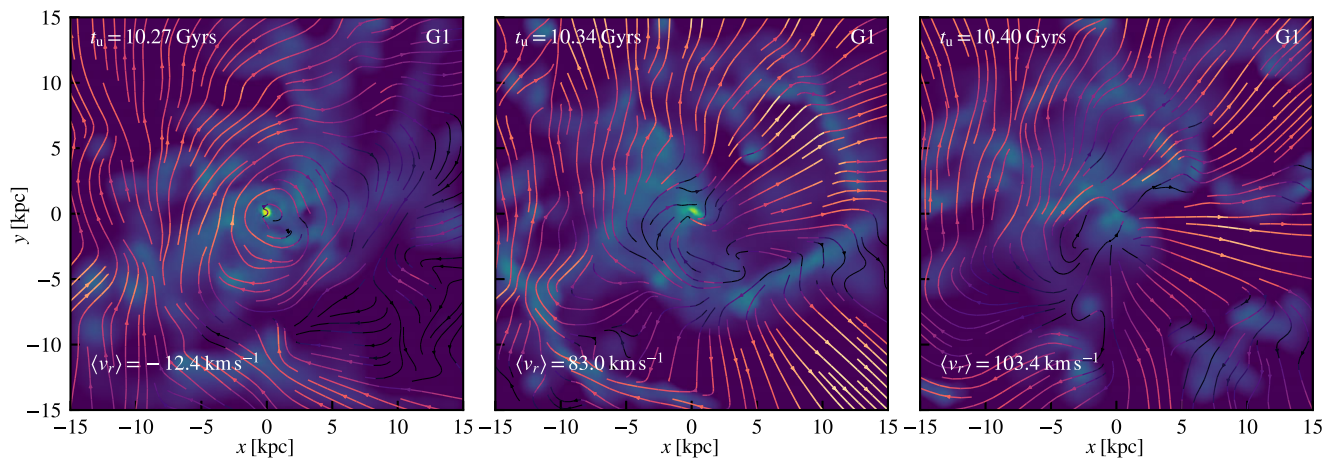
Figure 4. Surface density (colour scale) of the face-on gas content of halo G1, with each panel from left to right showing its distribution before, during and after the AGN outburst, respectively. Streamlines indicate the gas velocity with a colour intensity that is proportional to its magnitude. The average radial velocity of gas within a sphere of 30 kpc from the centre of halo G1 is shown in the lower left corner. The times at which the galaxy was imaged are indicated in the top left corners of each panel.

takes for the perturbation to grow ensures that the removal of the gas causes a maximal effect at larger distances from the centre.

To understand why this is the case, consider a system in which all particles are on circular orbits. When a central perturbation is exerted, the orbits of particles become elliptical and are able to come closer to the centre (contraction). When the perturbation is removed, particles that have descended down the perturbed potential well will have gained energy, allowing them to reach radii further beyond their original radius (expansion). Evidently, the picture is more nuanced in a more realistic scenario in which particles are neither necessarily on circular orbits nor in the same orbital phase. Nonetheless, this example helps illustrate the consequences of such perturbations.

Our interpretation implies that the degree of initial contraction and subsequent expansion must be related: A shell that responds strongly to the addition of a perturbation will initially contract and subsequently expand more than one with a weaker response. Thus, the amplitude of the expansion will, in part, be determined by how strong the initial contraction was. Secondly, the time-scale of the perturbation determines its effectiveness in altering the kinematics of a radial shell: If the duration of the perturbation is short compared to the dynamical time-scale of a given radial shell, particles do not have enough time to deviate significantly from their original orbits and change their energy. On the other hand, if the time-scale is sufficiently long, its effect becomes maximal.

To illustrate this, we investigate whether there is a correlation between the expansion and contraction of different radial shells of halo G1, as well as the dependence of their amplitude with distance from the centre of the halo. We identify the times at which the gravitational perturbation sourced by the gas disc starts ($t_{\rm pre\text{-}peak}$) and ends ($t_{\rm post\text{-}peak}$). We can thus measure the enclosed masses at these times relative to the time when they peaked ($t_{\rm peak}$), and thus estimate the degree of contraction and expansion of each shell. Although identifying $t_{\rm peak}$ and $t_{\rm post\text{-}peak}$ is straightforward, locating the time at which the perturbation starts is less so. By visually inspecting the evolution of the enclosed masses of DM (Fig. 3), we can estimate the time at which the halo starts contracting ($t_{\rm u} \sim 9$ Gyr). This coincides with the time when gas was being delivered to the central regions.

Once these times have been measured, the degree of expansion and contraction of each shell is estimated by taking the ratio of enclosed masses at different apertures, ranging from 1 to 20 kpc. This is
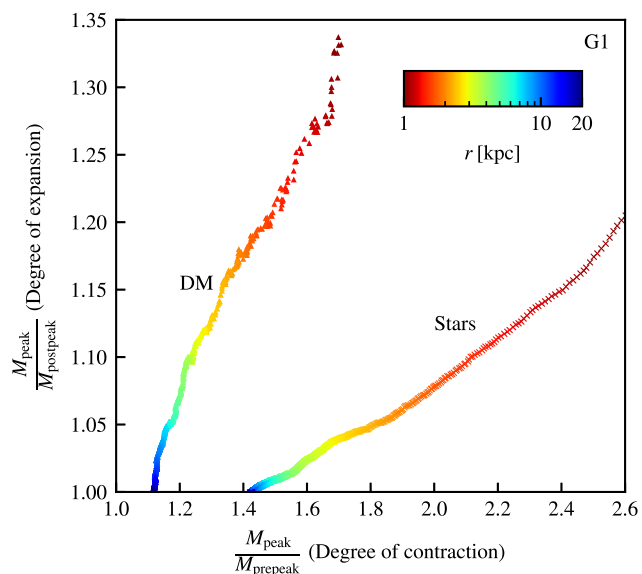

Figure 5. Degree of expansion (vertical axis) as a function of degree of contraction (horizontal axis), for different radial shells in the radius range, $1.0 \lesssim r/{\rm kpc} \lesssim 20.0$, for halo G1. We estimate the quantities by identifying the time at which the DM peaks and measure the mass prior to the peak, $M_{\rm pre\text{-}peak}$ ($t_{\rm u} \sim 9$ Gyr), and after the peak, $M_{\rm post\text{-}peak}$ ($t_{\rm u} \sim 10.3$ Gyr). These times are indicated in Fig. 3. The colour of each marker indicates the value of the spherical aperture.

shown in Fig. 5, which demonstrates that the degree of expansion is indeed related to the degree of contraction, as expected from our previous arguments. Furthermore, the amplitude increases towards the centre of the halo, with the DM component losing ∼25 per cent and ∼10 per cent within 1 and 3 kpc, respectively. Similarly, the expansion of the stellar component correlates well with the degree of contraction, although in a different manner compared to the DM component. Also worth noting is the offset from unity along the *x*-axis, likely caused by the growth of both the halo and the galaxy. This is a consequence of our definition of the degree of contraction, which includes the *total* mass increase. Their relative offset is explained by the fact that the galaxy grows more than the DM halo during

the time-scale under consideration. Finally, differences between the dynamical properties of the DM and stars might affect the degree of contraction caused by the gas, since circular orbits respond more strongly.

To ascertain how common AGN-fuelled blowouts are, we inspect the mass evolution of the gas, DM, and stars within 2 kpc from the centre of all MW-mass haloes. We then identify the times when the galaxy loses a large amount of gas in a short time-scale (less than 100 Myr, which corresponds to the time resolution of our data outputs) and inspect whether there is an associated decrease in the stellar and DM masses. To rule out a localized blowout that is not sufficiently strong to disrupt the gas disc, the gas content within 5 kpc should have also significantly decreased. Seven haloes out of the 45 studied here show definite evidence supporting that they experience such events at least once during their lifetime, with two others showing strong hints that they did. This comprises roughly 15 per cent to 20 per cent of the sample studied here, with the rest not experiencing such an event or having a complicated evolution that prevents us from making a definite statement on whether they have experienced one or not.

These findings are applicable to the real universe as long as strong AGN outbursts are able to completely remove the central gas content of galaxies. The parameters modulating their efficiency in EAGLE were calibrated by requiring that the model should reproduce a number of population statistics and scaling relations. Nonetheless, this is not the only prescription that meets these requirements. An example is the IllustrisTNG model, which includes a kinetic feedback mode at low mass accretion rates instead of the purely thermal implementation used in EAGLE. These modelling differences lead to different predictions for poorly constrained relations, such as how gas-rich the circumgalactic medium is as a function of halo mass below $\sim 10^{12}\ \mathrm{M}_\odot$ (Davies et al. 2020; Kelly et al. 2021). This suggests the EAGLE AGN model is more effective at removing baryons on the MW mass scale than other similarly realistic simulations. It would be interesting to examine whether AGN outbursts similar to the ones discussed above are also present in other simulations using different ways to model AGN feedback.

3.3 Stellar bars

In a number of MW-mass haloes we observe a decrease in the central mass of DM and stars taking place over several Gyr, as opposed to the AGN-induced gas blowouts, which correspond to Myr time-scales. This decrease occurs in haloes whose central regions are dominated by stars, with the largest decreases associated to strongly barred galaxies. The top panels of Fig. 2 show three such examples. Halos G1 and G2 have a global maximum in the enclosed DM mass followed by a monotonic decrease such that by $z = 0$, they have lost ~ 20 per cent and ~ 40 per cent of the peak DM mass within 2 kpc, respectively. This number excludes the initial, blowout-induced mass decrease observed in halo G1. By contrast, halo G3 shows a non-monotonic evolution of the central mass of DM and stars. This reflects the nature of its past evolutionary history, which is much more turbulent than for haloes G1 and G2. In contrast to these, which remained relatively undisturbed once the peak mass had been reached, halo G3 underwent several mergers and flybys by surrounding galaxies.

The development of a stellar bar in our simulations is associated with the outward transfer of stellar and DM mass. The evolution of bars is driven by the exchange of angular momentum with the surrounding components of the system (Athanassoula 2003). To measure the strength of the bar, we first orient the galaxy so that it is viewed face-on. This is achieved by aligning the spin of the stellar

component, computed by measuring the total angular momentum of all stars within 5 kpc from the centre, along the z-axis. The galaxy is then split into several concentric cylindrical annuli of 4 kpc in height and of variable width, such that each encloses 500 stellar particles. This choice provides better spatial resolution than bins of constant width in the barred regions, which contain more stellar particles than the outer regions. For each bin we measure the strength of the quadrupole moment of the azimuthal distribution of stellar particles, relative to their monopole strength:

$$A_2 \equiv \frac{\sqrt{a_2^2 + b_2^2}}{a_0}\,, \tag{2}$$

where

$$a_m = \sum_i^N M_i \cos m\phi_i\,, \tag{3}$$

$$b_m = \sum_i^N M_i \sin m\phi_i\,. \tag{4}$$

The sums are taken over all stellar particles in the bin, with M_i and ϕ_i their masses and azimuthal angles, respectively. Additionally, we also measure the quadrupole moment phase angle via $\phi_2 = 0.5 \arctan(b_2/a_2)$.

Finally, a Savitzky–Golay filter is used to smooth the radial variation of $A_2(r)$, with the length of the smoothing window set to 5 per cent of the total number of annuli. The right-hand panels of Fig. 6 show the $A_2(r)$ profile and the quadrupole moment phase angle for halo G2 at $z = 0$. The former has a prominent peak within 4 kpc associated with the presence of a strong bar, which shows a consistent orientation out to 4 kpc. We use the peak value, $A_2^{\max}$, to estimate the strength of the bar for each galaxy as a function of time. In this work, we use a threshold of $A_2^{\max} = 0.15$ to estimate when a bar forms, with the choice behind this value being strictly operational. Given that features and artefacts not related to bars can also boost the quadrupole moment in complicated cosmological simulations such as this one, we visually inspect the stellar distribution of galaxies with $A_2^{\max} \geq 0.15$ to confirm the presence of a bar.

Two other important properties of the bar are its length and pattern speed. To measure the length, we employ the definition adopted by Algorry et al. (2017): the radius at which $A_2(r)$ first drops below 0.15 after it has reached $A_2^{\max}$. The dashed black circle in the left-hand panel of Fig. 6 shows the extent of the bar determined in this way.

We measure the bar pattern speed directly by computing the change in the orientation of the bar between consecutive temporal outputs, i.e. $\Omega_p = \Delta\theta_p/\Delta t$. The angle of the bar, θ_p, is measured from the phase of the quadrupole moment at the radius where $A_2(r)$ peaks.

The bottom panels of Fig. 2 show the time evolution of the strength of the stellar bars in the galaxies illustrated on the top panels. The bars in both halo G1 and G2 form at around the time when the central DM mass begins to decrease. Once formed, the bars generally increase in strength monotonically. The evolutionary story of halo G3 is less trivial and the bar goes through periods of strengthening and weakening. At early times ($t_u \leq 7{-}7.5$ Gyr), the value of A_2 is large but in spite of this, we do not visually recognize a bar. The large value of A_2 is caused by mergers occurring along the line-of-sight, and by the fact that the centre becomes ill defined during this period. The end result is that the projected stellar distribution exhibits a large quadrupole moment. Additionally, transient elongations of the stellar distribution influence the values of $A_2^{\max}$, as seen in the variations of its value in the bottom panel of Fig. 2. The newly formed bar weakened significantly probably as a result of the rapid increase in the density of the central gas that preceded the AGN blowout. Interestingly, most of this gas was distributed along a
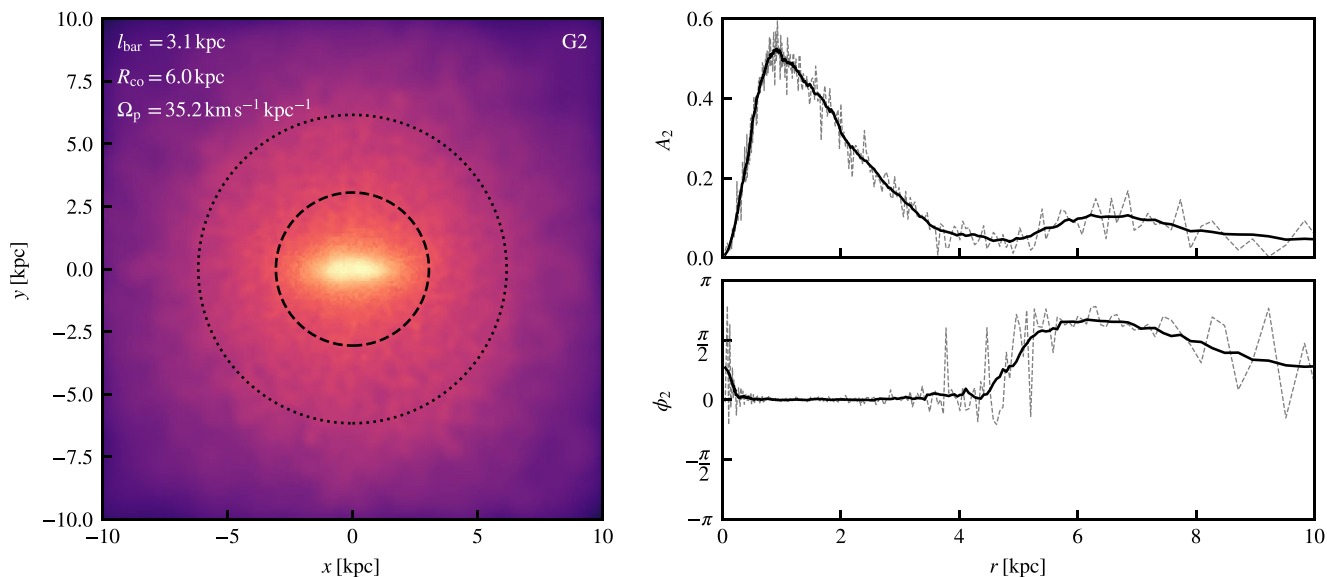
Figure 6. Left-hand panel: Logarithmic surface density (colour scale) of the face-on view of the stellar component of halo G2. The face-on orientation is chosen such that the bar is aligned along the x-axis. The values of the surface density range from 10^{10} to $10^5\,\mathrm{M}_\odot\,\mathrm{kpc}^{-2}$. The values of the bar length, pattern speed, and corotation radius are shown in the top-left corner. Its extent and corotation radius are also indicated by the dashed and dotted circles, respectively. Top-right panel: Radial variation of the $A_2(r)$ metric for halo G2 at $z = 0$. We use the peak value to characterize the strength of the bar. The dashed lines show the raw values obtained using cylindrical annuli 4 kpc in height, each enclosing 500 stellar particles. These values are smoothed using a Savitzky–Golay filter (black solid line). Bottom-right panel: Same as the panel above, but for the quadrupole moment phase angle.

bar-like feature aligned with the stellar bar. After increasing in strength again, there is an additional weakening episode that is likely caused by a merger event (Ghosh et al. 2021). In all three cases, the bars have significantly slowed down by $z = 0$, with the ratio of corotation radius to bar length equal to 2.1, 1.9, and 2.0 respectively.

For haloes G1 and G2 the secular decrease in the central DM mass is clearly associated with the formation and subsequent evolution of the bar. Nonetheless, even though both have strong bars of similar strengths at $z = 0$, each lost different amounts of mass from the central regions. This is due to the fact that the bars formed at different times and evolved by different amounts. To investigate further the connection between the decrease in central DM mass and the prominence of the stellar bar, the age of the bar should be taken into account. The metric we use is the average mass-loss rate between z_{peak} and $z = 0$, normalized by the peak DM mass within 2 kpc. We consider only those examples that exhibit a monotonic decrease in the central DM mass, e.g. haloes G1 and G2, but not G3. This selection was done by visually inspecting the central mass evolution of all the MW-mass haloes in the simulation. 23 out of the initial 45 haloes satisfy this criterion, which preferentially selects galaxies that have undergone a relatively undisturbed evolution after the peak in central DM mass was reached. Finally, we exclude sudden DM mass decreases associated with the gas blowouts discussed in the previous section, since here we are interested in the bar-driven secular decrease.

Fig. 7 shows the variation of the average fractional mass-loss rate between z_{peak} and $z = 0$ of each monotonically expanding halo as a function of their time-averaged bar strength, $\langle A_2^{\mathrm{max}} \rangle$.[2] This value was computed by averaging A_2^{max} from the time at which the enclosed DM peaked up to $z = 0$. The horizontal error bars indicate the variation of
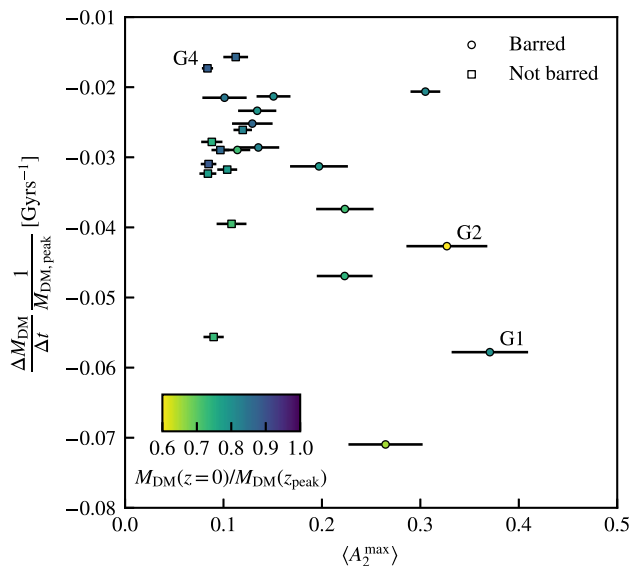

Figure 7. The time-averaged fractional mass-loss rate of haloes that exhibit a monotonically decreasing central DM mass as a function of their average bar strength. The average bar strength is computed from $z = 0$ until the time when the enclosed DM peaks. The circles show galaxies that have values of $A_2^{\mathrm{max}} \geq 0.15$ for longer than 1 Gyr. These are assigned to the sample of barred galaxies. Galaxies that do not satisfy this criterion are assigned to the unbarred population. The horizontal error bars show the spread in values of $A_2^{\mathrm{max}}(t)$ for each galaxy since t_{peak}, and indicate how much the quadrupole moment strength has evolved since then. Finally, each dot is coloured according to present-day to peak mass ratio, as indicated in the legend.

$A_2^{\mathrm{max}}(t)$, with low values corresponding to galaxies whose quadrupole moment strength remained relatively unchanged (e.g. if the stellar disc was axisymmetric throughout the simulation or the bar did not weaken or strengthen). We further classify galaxies into barred or

---

[2]The reason behind using the average bar strength instead of the $z = 0$ strength is that some of the galaxies had (weak) bars in the past that later dissolved.

unbarred depending on whether they had a value of A_2^{max} greater than 0.15 during at least 1 Gyr. This ensures that even galaxies that were barred in the past but are not at $z = 0$ are correctly identified, whilst excluding high, transient values of A_2^{max}.

Broadly speaking, Fig. 7 suggests that the stronger the time-averaged bar strength of a galaxy is, greater its secular DM mass-loss rate. To quantify this, we calculate Pearson's correlation coefficient $\mathcal{R}$ between $\langle A_2^{max} \rangle$ and the (average) fractional mass-loss rate for both populations. The median value for the barred sample is $\mathcal{R} = -0.7_{-0.2}^{+0.2}$, giving support to our previous claim. On the other hand, the unbarred sample has a median of $\mathcal{R} = 0.2_{-0.3}^{+0.3}$, which is consistent with no correlation. It is worth noting that the strongest correlation is found between how much the bar evolved over time and the time-averaged fractional mass-loss rate. The correlation coefficient between these two variables is $\mathcal{R} = -0.83 \pm 0.07$. The quoted uncertainties were obtained using a bootstrap technique.

Fig. 7 shows several other interesting features. First, a number of haloes with very low values of $\langle A_2^{max} \rangle$ have a wide range of mass-loss rates. These galaxies were never barred, and thus the expansion could not have been caused by a bar. We find that these galaxies were gas rich in the past, which caused the haloes to contract. As time progressed, star formation locked some of baryons in stars but the resulting supernovae feedback expelled gas from the central regions. As a result, the overall baryon mass decreased over time, leading to a slightly less contracted halo at later times. This reduction in the central baryon content takes place on much longer time-scales than the AGN phase. Secondly, the moderately barred galaxy above the G2 data point has a very low central mass-loss rate given its bar strength. As indicated by the horizontal error bars, there was very little change in A_2^{max} which remained roughly constant at $A_2^{max} \sim 0.3$ since its formation. This hints at the need for evolution in the strength of a bar for effective transfer of central DM mass outwards. Finally, to reiterate the importance of the time-scale over which the stellar bar acts, halo G1 experienced a greater mass-loss rate than halo G2 but lost less central DM mass. This is because G1 had a bar for $\sim$4 Gyr, whereas G2 had it for $\sim$10 Gyr.

Finally, many of the barred galaxies considered here also exhibit a decrease in the central mass of stars, although to a lesser extent than their DM content. This is observed in all three barred examples shown in the top panels of Fig. 2. The presence of a bar is expected to not only affect the DM, but also the stellar distribution. Whether particles near resonances are able to emit or absorb angular momentum is dependent on their dynamical properties. Spheroid components such as a DM halo or a stellar bulge are net absorbers of angular momentum, so one might expect the stellar bulge to be similarly affected. We have checked whether this is the case for halo G2 by classifying its $z = 2$ stars into bulge and disc components based on their circularities, $\epsilon_{circ} \equiv j_z/j_{z, circ}(E)$. By tracking a subset of the most bound particles of each component, we found that the stellar mass-loss within 2 kpc is dominated by expansion of the stellar bulge. The net effect is in line with the 'smoothing' effect that non-axisymmetric features have on the rotation and mass distribution curves of disc galaxies (Berrier & Sellwood 2015). Indeed, the rotation curves of these galaxies are strongly peaked at small radii when the bar initially formed but are less so as time progresses.

These findings are in qualitative agreement with those of Algorry et al. (2017), although there are differences between these studies. First, we analyse a higher resolution version of the EAGLE simulation, with an increase of almost one order of magnitude in the particle mass resolution. This allows us to study the evolution of the inner regions of haloes more confidently. On the other hand,

the smaller volume reduces the number of barred galaxies that we can study. Nonetheless, we are able to have a more detailed look at the evolution of the central regions of these haloes. This reveals the importance of the age of the bar, which is primarily determined by the assembly history of its halo. Even for galaxies with similar bar strength at $z = 0$, substantial differences in formation time alter how much the halo de-contracts. Moreover, we also note that the expansion of the DM halo is often accompanied by an expansion of the stellar component. Finally, Algorry et al. (2017) used a stellar mass criterion to select their sample, whereas we select ours based on the virial mass of the DM halo. In practice, this results in the stellar component of the haloes in our study being less massive than those in Algorry et al. (2017). This follows from the fact that in EAGLE the stellar mass function is underestimated (Schaye et al. 2015), so one has to consider more massive haloes to find sufficiently massive galaxies.

3.4 Halo contraction

All the haloes considered in this study end up having a higher central density compared to their DMO counterparts. This is a consequence of the accumulation of baryonic mass resulting from the dissipational collapse of gas during the assembly of the galaxy, the so-called adiabatic contraction (Barnes & White 1984; Blumenthal et al. 1986; Cautun et al. 2020). This trend is opposed by the processes we have discussed here which reduce the central DM density. We now consider how the bar-driven secular evolution of a galaxy alters the degree of contraction of its host halo, bearing in mind that the degree of contraction depends on the halo assembly history (Abadi et al. 2010).

An illustrative example is halo G2, which had the strongest and longest lived bar in our sample. This galaxy formed 50 per cent of its stars by $z = 2.6$ and was left largely undisturbed for a large fraction of the age of the universe. Changes to its density profile are solely driven by internal, secular processes such as the influence of its stellar bar. To estimate how contracted the halo is relative to its DM counterpart, we follow the procedure described by Abadi et al. (2010). First, we define a shell of radius, R_i, in the DMO simulation that encloses a given amount of DM, rescaling the particle masses: $M_{DM}^{DMO}(< R_i) = (1 - f_b)M_{tot}^{DMO}(< R_i)$. We then find the corresponding radius, R_f, in the hydrodynamical simulation that encloses the same amount of DM, i.e. $M_{DM}^{hydro}(< R_f) = M_{DM}^{DMO}(< R_i)$. In practice, this amounts to enclosing equal numbers of DM particles for each shell. Once these two radii have been found, we measure the total enclosed masses, $M_{tot} = M_{DM} + M_b$, for each, where M_b is the mass of baryons. The ratio R_f/R_i measures the degree of contraction ($R_f/R_i < 1$) or expansion ($R_f/R_i > 1$) of a radial shell as a function of the increase ($M_{tot}^i/M_{tot}^f < 1$) or decrease ($M_{tot}^i/M_{tot}^f > 1$) of total mass contained within it. This allows a straightforward comparison to the predictions of the simple adiabatic contraction model, for which $R_i M_{tot}^i = R_f M_{tot}^f$.

Fig. 8 shows how these ratios vary as a function of time for halo G2, as well as for an unbarred galaxy with a very small reduction in its central DM content. The values are only shown for shells with radii larger than the Power et al. (2003) convergence radius of the DMO halo, with each shell containing 100 more DM particles than the previous one. For consistency when comparing the evolution between the chosen haloes, only the last $\sim$6 Gyr of the simulation outputs are shown. Consequently, the evolution of halo G2 is larger than shown in here, since its expansion began at $t_u \sim 4$ Gyr. Nonetheless, it is evident that its contraction evolves strongly with time. This is in
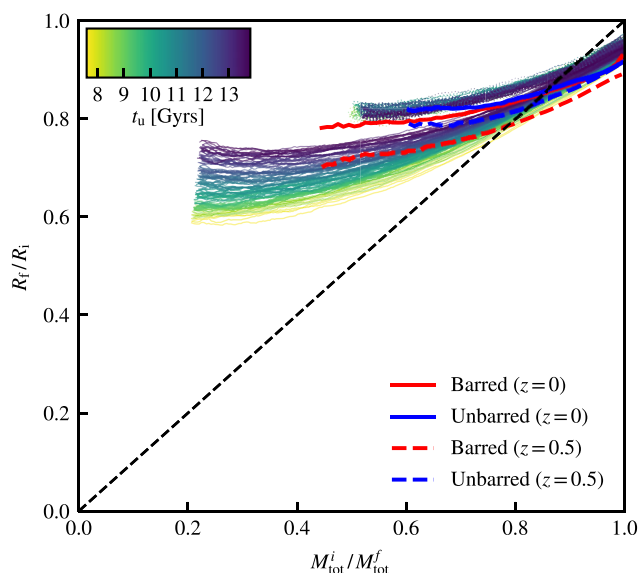
Figure 8. Response of the DM halo to the assembly of the galaxy at its centre. The ratio R_f/R_i is shown as a function of the change in enclosed total mass $M_{\rm tot}^i/M_{\rm tot}^f$ at several times for halo G2 (solid coloured lines) and a halo hosting an unbarred galaxy (similar to G4; dotted coloured lines). The values are only shown for radial shells with radii larger than the convergence radius defined by (Power et al. 2003), which is different for each halo. For a consistent comparison, we show only values measured at $t_u \geq 7.5$ Gyr. The solid and dashed lines show the $z = 0$ and $z = 0.5$ average values for the barred (red) and unbarred (blue) sample of haloes shown in Fig. 7, respectively. The average only includes haloes that are relaxed. We do not show the average value for $M_{\rm tot}^i/M_{\rm tot}^f \leq 0.45$ (0.60) because only a small number of haloes hosting barred (unbarred) galaxies reach these low values. The diagonal dashed line shows the prediction of the adiabatic contraction model.

contrast to the unbarred halo, which remains virtually unchanged over the plotted time period.

As discussed in other studies (e.g. Abadi et al. 2010; Cautun et al. 2020), the adiabatic contraction model overestimates the degree of contraction in the central regions. We find that it also underpredicts it at larger radii as a result of baryonic outflows. Consider a radial shell at the virial radius of the halo, R_{200}. At such large distances, contraction should be negligible and thus $R_f/R_i \sim 1$. Under the assumption of no DM shell mixing, the values of $M_{\rm tot}^{\rm DMO}(< R_i)$ and $M_{\rm tot}^{\rm hydro}(< R_f)$ only depend on the enclosed baryonic mass. For the collisionless case, this is simply $M_b^{\rm DMO}(< R_i) = f_b M_{\rm tot}^{\rm DMO}(< R_i)$. However, if feedback expels baryons beyond the virial radius, then the baryon fraction at such a distance is less than the cosmic baryon fraction. In other words, $M_b^{\rm DMO}(< R_i) \geq M_b^{\rm hydro}(< R_f)$ and thus $M_{\rm tot}^{\rm DMO}(< R_i)/M_{\rm tot}^{\rm hydro}(< R_f) \geq 1$. Evidently, this is violated if there is a reduction in the enclosed DM mass at a fixed physical aperture caused by the reduced growth of the halo associated with the loss of baryons at early times, as discussed by Sawala et al. (2013). However, this is not the case for MW-mass haloes in the EAGLE simulations (Schaller et al. 2015).

Focusing on the sample of monotonically expanding haloes, Fig. 8 also shows how the average values of the two ratios plotted change between $z = 0.5$ (red) and $z = 0$ (black). When computing the averages, only relaxed haloes are included. To identify relaxed haloes we adopt the most restrictive condition proposed by Neto et al. (2007): The centre of mass should be offset from the centre of potential by less than $0.07R_{\rm vir}$. We only show the averages for

$M_{\rm tot}^i/M_{\rm tot}^f \geq 0.45$ (0.60) for the barred (unbarred) sample, since very few haloes reach smaller values. The barred sample is, on average, more contracted than the unbarred one as a consequence of their more massive stellar components. The average contraction of each population has decreased over time; the evolution of the unbarred sample is less than that of the barred one.

The systematic shift in the average contraction of the haloes in our sample is due to the secular processes discussed earlier. Since one of the driving effects is stellar bars, which transfer angular momentum from the stars to the DM particles (see Appendix A), this process could lead to different DM particle distribution functions in haloes whose central galaxies have a bar compared to those which do not. These differences may be relevant for distribution function-based models of halo contraction (e.g. Callingham et al. 2020).

Finally, there is considerable halo-to-halo scatter introduced by several factors such as the mass of the central galaxy, the assembly history, the orbital distribution of DM particles, etc. Among these, AGN-driven blowouts could also play a role due to their stochastic nature. Given the small size of our halo sample, we can only note this trend which needs to be confirmed by larger simulations.

4 DISCUSSION AND CONCLUSIONS

In this work, we have studied the evolution of the central distribution of DM in simulated MW-mass haloes, drawn from a ΛCDM cosmological hydrodynamics simulation. Specifically, we have investigated how the mass within the inner 2–5 kpc is affected by processes associated with the growth of the central galaxy in the halo. We analysed 45 haloes taken from the high-resolution version of the EAGLE simulation, selected by requiring that their final mass, M_{200}, be similar to that of the MW at $z = 0$.

As in previous studies, we find that, at the present day, the haloes are more centrally concentrated than their counterparts in a DMO simulation. However, the degree of contraction is significantly less than expected in the simple adiabatic contraction model (Blumenthal et al. 1986) and its refinements (Gnedin et al. 2004; Cautun et al. 2020). We also find that there are times during the evolution of a halo when its central DM mass decreases, although it always remains more massive than its DMO twin. We have identified two main processes responsible for lowering the central DM mass.

The first is AGN-induced gas blowouts. These events involve gas that had slowly become so dense so as to become gravitationally dominant in the central regions. As the gas is violently expelled, the central regions of the haloes expand in a process analogous to that discussed by Navarro et al. (1996a). Both DM and stars participate in the expansion. Interestingly, we find that these blowouts can reduce the enclosed DM and stellar mass at radii much larger than those in which the gas is gravitationally dominant. Although it is clear that the effect of the blowouts fades away at larger distance, we hypothesize that the very long time-scales of the gravitational perturbations caused by the gas before being blown out are responsible of this effect. In all cases, the initial inflow of gas occurs during or shortly after an interaction with a nearby galaxy.

The second process that causes the central halo regions to expand is a bar-mediated transfer of angular momentum. This transfer reduces the central DM density at a rate that is likely set by the time-averaged stellar bar strength. The net change in the central DM density depends on the length of time since the bar formed.

The effects of AGN-driven gas blowouts and bar-driven angular momentum transfer that we have investigated in this work are not confined to the central regions of the haloes and can be seen out to

at least 5 kpc from the centre. Here, we have focused attention on the inner 2 kpc since this radius lies in the well-converged region as judged by the Power et al. (2003) criterion ($r_{power} \sim 1.5$–1.75 kpc).

Not all the galaxies in our sample undergo the two processes just described. As Fig. 2 shows, there is significant halo-to-halo scatter due to a variety of factors including differences in the assembly history of the halo, the central mass of the galaxy and likely the orbital distribution of DM particles. Roughly 30 per cent of the studied sample host bars. About 15 per cent to 20 per cent of our MW-mass haloes have experienced at least one AGN blowout capable of reducing their central stellar and DM densities. This is likely to be a lower limit, as we focus on haloes with well-defined evolutionary histories. At high redshifts, when the haloes and galaxies are assembled, it is difficult to assess the importance of the AGN blowouts.

While the reduction in central DM mass due to the presence of stellar bars similar to those that form in EAGLE is likely to be generic, the reduction caused by AGN-driven blowouts is expected to be specific to the EAGLE subgrid model. It would be interesting to explore if similar effects are present in other hydrodynamics simulations.

The processes discussed in our paper indicate that the assembly of baryons in MW-size haloes induces a complicated reaction in the DM halo. The degree of DM contraction in these haloes cannot be solely characterized by the present-day baryonic distribution, but by their complicated past evolutionary history. Our own MW contains two of the ingredients that source the complexity highlighted in our study: a stellar bar and a supermassive black hole at the centre. Our results suggest that unless the baryonic effects described in our paper are taken into account, studies that rely on contraction-based models, such as mass estimates of the MW, or direct or indirect searches of DM, could contain biases that are very difficult to account for.

ACKNOWLEDGEMENTS

DATA AVAILABILITY

Instructions on how to access the EAGLE data base that contains the data used in this paper can be found at http://icc.dur.ac.uk/data/, which is actively mantained by John Helly (Institute for Computational Cosmology, Durham University).

REFERENCES

Abadi M. G., Navarro J. F., Steinmetz M., Eke V. R., 2003, ApJ, 597, 21
Abadi M. G., Navarro J. F., Fardal M., Babul A., Steinmetz M., 2010, MNRAS, 407, 435
Agnello A., Evans N. W., 2012, ApJ, 754, L39
Algorry D. G. et al., 2017, MNRAS, 469, 1054
Artale M. C., Pedrosa S. E., Tissera P. B., Cataldi P., Di Cintio A., 2019, A&A, 622, A197
Athanassoula L., 2003, Galaxies and Chaos. Springer, Berlin, p. 313
Athanassoula E., 2013, in Falcon-Barroso J., Knapen J. H., eds, Secular Evolution of Galaxies. Cambridge Univ. Press, Cambridge, p. 305
Barnes J., White S. D. M., 1984, MNRAS, 211, 753
Benitez-Llambay A., Frenk C., 2020, MNRAS, 498, 4887
Benítez-Llambay A., Frenk C. S., Ludlow A. D., Navarro J. F., 2019, MNRAS, 488, 2387
Berentzen I., Athanassoula E., Heller C. H., Fricke K. J., 2004, MNRAS, 347, 220
Berrier J. C., Sellwood J. A., 2015, ApJ, 799, 213
Binney J., Gerhard O. E., Stark A. A., Bally J., Uchida K. I., 1991, MNRAS, 252, 210
Blumenthal K. A., Barnes J. E., 2018, MNRAS, 479, 3952
Blumenthal G. R., Faber S. M., Flores R., Primack J. R., 1986, ApJ, 301, 27
Booth C. M., Schaye J., 2009, MNRAS, 398, 53
Bozorgnia N. et al., 2016, J. Cosmol. Astropart. Phys., 2016, 024
Bozorgnia N., Bertone G., 2017, Int. J. Mod. Phys. A, 32, 1730016
Burkert A., 1995, ApJ, 447, L25
Buta R. J. et al., 2015, ApJS, 217, 32
Callingham T. M. et al., 2019, MNRAS, 484, 5453
Callingham T. M., Cautun M., Deason A. J., Frenk C. S., Grand R. J. J., Marinacci F., Pakmor R., 2020, MNRAS, 495, 12
Calore F. et al., 2015, J. Cosmol. Astropart. Phys., 2015, 053
Cautun M. et al., 2020, MNRAS, 494, 4291
Ceverino D., Klypin A., 2007, MNRAS, 379, 1155
Chan T. K., Kereš D., Oñorbe J., Hopkins P. F., Muratov A. L., Faucher-Giguère C.-A., Quataert E., 2015, MNRAS, 454, 2981
Crain R. A. et al., 2015, MNRAS, 450, 1937
Dalla Vecchia C., Schaye J., 2012, MNRAS, 426, 140
Davies J. J., Crain R. A., Oppenheimer B. D., Schaye J., 2020, MNRAS, 491, 4462
Davis M., Efstathiou G., Frenk C. S., White S. D. M., 1985, ApJ, 292, 371
Debattista V. P., Mayer L., Carollo C. M., Moore B., Wadsley J., Quinn T., 2006, ApJ, 645, 209
Di Cintio A., Brook C. B., Macciò A. V., Stinson G. S., Knebe A., Dutton A. A., Wadsley J., 2014, MNRAS, 437, 415
Dubinski J., Berentzen I., Shlosman I., 2009, ApJ, 697, 293
Dutton A. A. et al., 2016, MNRAS, 461, 2658
Dwek E. et al., 1995, ApJ, 445, 716
Einasto J., 1965, Tr. Astrofizicheskogo Inst. Alma-Ata, 5, 87
El-Zant A., Shlosman I., Hoffman Y., 2001, ApJ, 560, 636
El-Zant A. A., Hoffman Y., Primack J., Combes F., Shlosman I., 2004, ApJ, 607, L75
Eskridge P. B. et al., 2000, AJ, 119, 536
Fanali R., Dotti M., Fiacconi D., Haardt F., 2015, MNRAS, 454, 3641
Ghosh S., Saha K., Di Matteo P., Combes F., 2021, MNRAS, 502, 3085
Gnedin O. Y., Kravtsov A. V., Klypin A. A., Nagai D., 2004, ApJ, 616, 16
He Q. et al., 2020, MNRAS, 496, 4717
Hohl F., 1971, ApJ, 168, 343
Holley-Bockelmann K., Weinberg M., Katz N., 2005, MNRAS, 363, 991
Kataria S. K., Das M., 2019, ApJ, 886, 43
Kelly A. J., Jenkins A., Deason A., Fattahi A., Grand R. J. J., Pakmor R., Springel V., Frenk C. S., 2021, preprint (arXiv:2106.08618)
Laporte C. F. P., White S. D. M., Naab T., Ruszkowski M., Springel V., 2012, MNRAS, 424, 747
Łokas E. L., Ebrová I., del Pino A., Sybilska A., Athanassoula E., Semczuk M., Gajda G., Fouquet S., 2016, ApJ, 826, 227
Ludlow A. D. et al., 2017, Phys. Rev. Lett., 118, 161103
Lynden-Bell D., 1979, MNRAS, 187, 101
Lynden-Bell D., Kalnajs A. J., 1972, MNRAS, 157, 1
Martinez-Valpuesta I., Aguerri J. A. L., González-García A. C., Dalla Vecchia C., Stringer M., 2017, MNRAS, 464, 1502
Martizzi D., Teyssier R., Moore B., 2013, MNRAS, 432, 1947

Mashchenko S., Couchman H. M. P., Wadsley J., 2006, Nature, 442, 539

Miller R. H., Prendergast K. H., Quirk W. J., 1970, ApJ, 161, 903

Moster B. P., Naab T., White S. D. M., 2013, MNRAS, 428, 3121

Navarro J. F. et al., 2004, MNRAS, 349, 1039

Navarro J. F., Eke V. R., Frenk C. S., 1996a, MNRAS, 283, L72

Navarro J. F., Frenk C. S., White S. D. M., 1996b, ApJ, 462, 563

Navarro J. F., Frenk C. S., White S. D. M., 1997, ApJ, 490, 493

Ness M. et al., 2016, ApJ, 819, 2

Neto A. F. et al., 2007, MNRAS, 381, 1450

Noguchi M., 1987, MNRAS, 228, 635

Oh S.-H. et al., 2015, AJ, 149, 180

Planck Collaboration I, 2014, A&A, 571, A1

Pontzen A., Governato F., 2014, Nature, 506, 171

Power C., Navarro J. F., Jenkins A., Frenk C. S., White S. D. M., Springel V., Stadel J., Quinn T., 2003, MNRAS, 338, 14

Read J. I., Gilmore G., 2005, MNRAS, 356, 107

Ryden B. S., Gunn J. E., 1987, ApJ, 318, 15

Saha K., Martinez-Valpuesta I., Gerhard O., 2012, MNRAS, 421, 333

Sand D. J., Treu T., Ellis R. S., 2002, ApJ, 574, L129

Sanders R. H., Huntley J. M., 1976, ApJ, 209, 53

Sawala T., Frenk C. S., Crain R. A., Jenkins A., Schaye J., Theuns T., Zavala J., 2013, MNRAS, 431, 1366

Schaller M. et al., 2015, MNRAS, 451, 1247

Schaller M. et al., 2016, MNRAS, 455, 4442

Schaye J., 2004, ApJ, 609, 667

Schaye J., Dalla Vecchia C., 2008, MNRAS, 383, 1210

Schaye J. et al., 2015, MNRAS, 446, 521

Sellwood J. A., 2006, ApJ, 637, 567

Sellwood J. A., 2008, ApJ, 679, 379

Sheth K. et al., 2008, ApJ, 675, 1141

Skibba R. A. et al., 2012, MNRAS, 423, 1485

Somerville R. S., Davé R., 2015, ARA&A, 53, 51

Springel V., 2005, MNRAS, 364, 1105

Springel V., White S. D. M., Tormen G., Kauffmann G., 2001, MNRAS, 328, 726

Springel V., Di Matteo T., Hernquist L., 2005, MNRAS, 361, 776

Strigari L. E., Frenk C. S., White S. D. M., 2010, MNRAS, 408, 2364

Tollet E. et al., 2016, MNRAS, 456, 3542

Umetsu K., Diemer B., 2017, ApJ, 836, 231

Walker M. G., Peñarrubia J., 2011, ApJ, 742, 20

Wang J., Bose S., Frenk C. S., Gao L., Jenkins A., Springel V., White S. D. M., 2020, Nature, 585, 39

Weiland J. L. et al., 1994, ApJ, 425, L81

Weinberg M. D., Katz N., 2002, ApJ, 580, 627

Weinberg M. D., Katz N., 2007a, MNRAS, 375, 425

Weinberg M. D., Katz N., 2007b, MNRAS, 375, 460

White S. D. M., Rees M. J., 1978, MNRAS, 183, 341

Wiersma R. P. C., Schaye J., Smith B. D., 2009, MNRAS, 393, 99

Zavala J., Okamoto T., Frenk C. S., 2008, MNRAS, 387, 364

APPENDIX A: ANGULAR MOMENTUM EVOLUTION

Stellar bars mediate the transfer of angular momentum between different components of the system, with the net flow dependent on the morphology of the latter. We investigate this in the context of this work by tracking a subset of the most bound stellar and DM particles belonging to halo G2. This criterion selects particles which
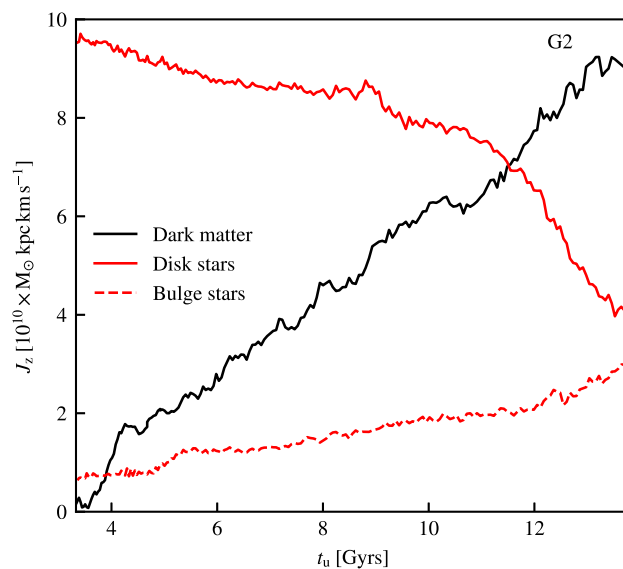

Figure A1. Angular momentum evolution of the component parallel to the stellar disc spin for the ($z = 2$) 5000 most bound particles of each of the components of halo G2. This is shown for disc and bulge stars by the red solid and red dashed lines, respectively. The black line corresponds to the DM component, smoothed using a linear Savitzky–Golay filter.

occupy the central regions of the system, where the effect of the bar will be the strongest.

We classify stellar particles as bulge or disc-like using the method of Abadi et al. (2003), which is based on their circularity parameters:

$$\epsilon_{circ} \equiv \frac{J_z}{J_{z,circ}(E)}.$$

J_z is the angular momentum component parallel to the stellar disc spin and $J_{z,circ}(E)$ is that of a circular orbit with the same binding energy. Thus, ϵ_{circ} ranges from $+1$ for corotating circular orbits to -1 for counter-rotating ones. $J_{z,circ}(E)$ is obtained by computing the binding energy and J_z of all stars in the system. Only certain regions in this phase space are accessible, with its bounds corresponding to $J_{z,circ}(E)$. Here we assign particles with $\epsilon_{circ} \geq 0.9$ to the disc, and those with $\epsilon_{circ} \leq 0.5$ to the bulge.

Finally, we identify the ($z = 2$) 5000 most bound particles of each of the components present in halo G2. This is just before its stellar bar formed. We then track the same particles over time and follow the evolution of their angular momentum component parallel to that of the stellar disc spin. This is shown in Fig. A1. We see that the disc subset steadily loses angular momentum, whereas the DM and bulge gain it, as expected. Given that we track a subset of the whole system, this is not a closed system and thus angular momentum is not strictly conserved. There are likely other sources of angular momentum not accounted for in this analysis, such as newly formed stars and the gas disc. Nonetheless, this gives a qualitative view on how angular momentum is redistributed by the bar.

This paper has been typeset from a TEX/LATEX file prepared by the author.